Applied Catalysis B: Environmental 306 (2022) 121110

Contents lists available at ScienceDirect

Applied Catalysis B: Environmental

journal homepage: www.elsevier.com/locate/apcatb

Persistent radical cation sp^2 carbon-covalent organic framework for photocatalytic oxidative organic transformations

Yuan-Zhe Cheng [a,c], Wenyan Ji [a], Xianxin Wu [b,c], Xuesong Ding [a,*], Xin-Feng Liu [b,c,**], Bao-Hang Han [a,c,**]

[a] CAS Key Laboratory of Nanosystem and Hierarchical Fabrication, CAS Center for Excellence in Nanoscience, National Center for Nanoscience and Technology, Beijing 100190, China
[b] CAS Key Laboratory of Standardization and Measurement for Nanotechnology, CAS Center for Excellence in Nanoscience, National Center for Nanoscience and Technology, Beijing 100190, China
[c] University of Chinese Academy of Science, Beijing 100049, China

ARTICLE INFO

Keywords:
Sp^2 carbon-covalent organic framework
Photoinduced radical material
Photocatalyst
Charge separation and recombination
Porous organic polymer

ABSTRACT

Persistent radical covalent organic frameworks (COFs) have exhibited great application potential in the fields of photocatalysis, magnetism, and biology. However, there is still a lack of a simple, green, and effective way to produce persistent radical COFs. Here, we synthesized two sp^2 carbon-covalent organic frameworks (sp^2C-COFs) with persistent triphenylamine radical cation ($TPA^{+\bullet}$), which can be generated by simple light irradiation since the effective donor–acceptor heterojunction is formed in ordered skeleton. The number of persistent $TPA^{+\bullet}$ will increase with the intensity of light irradiation and the photogenerated electrons generated simultaneously can be consumed by O_2 to form reactive oxygen species, which can be then used to carry out the oxidative organic transformations under visible light. In addition, femtosecond-transient absorption spectra prove that the difference in the structure of the two radical cation sp^2C-COFs will significantly influence the charge recombination rate, so that the materials show different catalytic efficiency.

1. Introduction

Covalent organic frameworks (COFs) possessing designable ordered porous structures show a huge potential for applications in gas absorption and separation, energy storage, sensing, optoelectronics, catalysis, and other fields [1]. Notably, most COFs are connected by reversible bonds such as imine or boroxine bonds. This reversible feature allows the mismatched bonds to be broken for correction in the process of synthesis, and ultimately form COFs with excellent crystallinity under thermodynamical control [2]. However, these reversible bonds also enable COFs to be easily hydrolyzed and collapsed in acidic/aqueous media, which greatly limits their further application [3].

Recently, several sp^2 carbon-COFs (sp^2C-COFs) with high chemical and thermal stability have been reported [4,5]. According to the previous literature, the structures and properties of sp^2C-COF will keep constant at harsh condition such as in aqueous HCl solution, aqueous NaOH solution, and most organic reagents [3]. The development of sp^2C-COFs certainly provides a way for solving the issues of COFs' stability. This breakthrough has laid a solid foundation for a bright future for COFs. However, the formation of refined crystalline structure linked by irreversible C=C bond is really a challenge, and only a few sp^2C-COFs have been reported so far [6–8]. Therefore, the exploration of the structure–activity relationship and furthermore application of sp^2C-COFs is still insufficient [9–11].

It is worth noting that in addition to the intrinsic robustness of the non-polarized C=C linkages, these special joints can also greatly promote the charge carrier delocalization [12,13], thereby endowing sp^2C-COFs with fascinating semiconductor properties and applications in light emission, photocatalysis, *etc* [14–16]. In general, delocalized electrons as a type of charge carrier are extremely easy to be excited and can be subsequently transferred to the catalytic site in a typical donor–acceptor (D–A) structure. Considering these D–A materials with a special electronic structure, we hypothesize that the persistent radical cation species could be formed in COFs by photoinduced electron transfer (PET) process in D–A structure [17]. The nature of the rigid-structured skeleton of COF protects the radicals from coupling

* Corresponding author.
** Corresponding authors at: University of Chinese Academy of Science, Beijing 100049, China.
E-mail addresses: dingxs@nanoctr.cn (X. Ding), liuxf@nanoctr.cn (X.-F. Liu), hanbh@nanoctr.cn (B.-H. Han).

https://doi.org/10.1016/j.apcatb.2022.121110
Received 13 October 2021; Received in revised form 29 December 2021; Accepted 16 January 2022
Available online 19 January 2022

quench, which stabilizes the radicals and prolongs their lifetime. In addition, this radical is produced by light stimulation, its initiation is simple and pollution-free. According to previous reports, persistent radical COFs can be obtained by following methods. (1) Radical molecules are connected into channels in COFs by post-synthetic functionalization or embedded into skeleton as building blocks [18,19]. (2) Radicals are formed in the non-radical COFs by the treatment of dopants such as iodine or tetracyanoquinodimethane (TCNQ) [4,20]. (3) Special units, such as diquat cations or 2,3,5,6-tetrachlorophenylmethane, in COFs can be converted into radical form by oxidation or reduction reactions [21–23]. However, these preparation methods of persistent radical COFs are complicated. So far, there is still a lack of a simple, efficient, and green way to directly generate radical in the structure. Meanwhile, it is well-known that the COFs themselves possess an excellent conjugated structure that could generate and stabilize radicals owing to ordered electronic structure and extended rigid skeleton. Therefore, it can be expected that by carefully designing the electronic structure of sp^2C-COFs, persistent radicals can be spontaneously generated in the skeleton during the preparation of COFs in response to mild external stimulation such as light irradiation.

Here, we designed and synthesized two sp^2C-COFs using the typical electron-rich monomer (triphenylamine) and the electron-deficient monomer (triazine ring) to form effective D–A structure in crystalline skeleton, named TPA-sp^2C-COF and TBPA-sp^2C-COF, respectively. The obtained materials possess interesting properties that the signal of persistent TPA radical cation ($TPA^{+\bullet}$) can be detected by electron paramagnetic resonance spectroscopy (EPR). The amount of $TPA^{+\bullet}$ increase from 6.8% to 10.7% with the introduction of external light stimulation intensity, and this phenomenon proves that these sp^2C-COFs are a typical photoinduced radicals (PIR) materials [24]. As far as we know, this is the first report of PIR COFs. According to further studies, as compared with TPA-sp^2C-COF, the charge separation and charge recombination process of the TBPA-sp^2C-COF are further adjusted by constructing through-bond energy transfer (TBET) system proved by femtosecond-transient absorption (fs-TA) spectra. Benefiting from the effective charge separation and charge recombination process and the high-energy photogenerated electrons, reactive oxygen species (ROS) can be formed from O_2 and used for photocatalytic reaction in this work. The formation of these radicals in these sp^2C-COFs is well explained and demonstrated as follows, $TPA + h\nu \rightarrow TPA^* + O_2 \rightarrow TPA^{+\bullet} + O_2^{-\bullet}$ [25]. With the introduction of oxygen atmosphere, the amount of $TPA^{+\bullet}$ will further increase to 13.2%. These COFs have been successfully used as catalysts in the photocatalytic reaction of oxidative hydroxylation of aryl boronic acids into phenols. This is the first time that the traditional reaction can be achieved in air at room temperature and without any assistance of co-catalysts or metals. In addition, the wide applicability of these sp^2C-COFs for photocatalysis has been verified, and the TBPA-sp^2C-COF exhibits excellent catalytic activity in photocatalytic cross-dehydrogenative coupling reaction and the C-3 functionalization reaction of indoles. Overall, these radical cation sp^2C-COFs as catalysts have demonstrated excellent compatibility of substrates and the universality of photocatalytic reaction, which provides a reference for the preparation of crystalline porous materials with high performance.

2. Experimental methods

2.1. Synthesis of sp^2C-COFs

2.1.1. Synthesis of TPA-sp^2C-COF

A Teflon-lined steel autoclave (25 mL) was charged with tris(4-formylphenyl)-amine (TPA) (65.9 mg, 0.2 mmol), methanol (8 mL), and *o*-dichlorobenzene (*o*-DCB) (8 mL). (Caution: All liquid chemicals were bubbled with nitrogen for 15 min). The above mixture was stirred under nitrogen, and then 2,4,6-trimethyl-1,3,5-triazine (TMT) (24.6 mg, 0.2 mmol) and NaOH (35.0 mg, 99.9% metal basis) were added into the autoclave. The final mixture was bubbled with nitrogen for 10 min, and then sealed and placed in a preheated oven at 180 °C for three days. Then, the autoclave was cooled down slowly, and the formed precipitate was collected by centrifugation. The product was then washed gradiently with a mixed solution of methanol, dichloromethane, and *n*-hexane in the order that the polarity of the mixed solvent gradually decreased. The obtained product was gradually heated from room temperature to 120 °C in a nitrogen stream for drying to give an orange powder with yield of 81%. Elemental analysis: calculated C (81.41%), H (4.52%), N (14.07%) and observed C (66.84%), H (4.62%), N (11.22%).

2.1.2. Synthesis of TBPA-sp^2C-COF

A Teflon-lined steel autoclave (25 mL) was charged with [1,1′-biphenyl]-4-carboxaldehyde (TBPA) (111.5 mg, 0.2 mmol), methanol (4 mL) and *o*-DCB (12 mL) (Caution: All liquid chemicals were bubbled with nitrogen for 15 min). The above mixture was stirred under nitrogen, and then TMT (24.6 mg, 0.2 mmol) and NaOH (35.0 mg, 99.9% metal basis) were added into the autoclave. The final mixture was bubbled with nitrogen for 10 min, and then sealed and placed in a preheated oven at 180 °C for three days. Then, the autoclave was cooled down slowly, and the formed precipitate was collected by centrifugation. The product was then washed gradiently with a mixed solution of methanol, dichloromethane, and *n*-hexane in the order that the polarity of the mixed solvent gradually decreased. The obtained product was gradually heated from room temperature to 120 °C in a nitrogen stream for drying to give a yellow-green powder with yield of 78%. Elemental analysis: calculated C (86.26%), H (4.79%), N (8.95%) and observed C (74.24%), H (4.63%), N (7.37%).

2.2. General procedure for hydroxylation of arylboronic acids

A 5 mL flask was charged with *N*,*N*-dimethylformamide (DMF) (5 mL), arylboronic acids (0.5 mmol), and photocatalyst (4 mol% based on monomer). The mixture was open to air in the flask and magnetically stirred at room temperature under irradiation of 23 W white LED lamp at a distance around 8 cm. After 48 h, the reaction was quenched by addition of aqueous HCl solution (6 mL, 10%). The resultant solution was extracted with diethyl ether (3 × 5 mL). The combined organic phase was washed with brine (10 mL) and dried over Na_2SO_4. After being concentrated *in vacuo*, a solution of diethyl ether layer (200 μL) was added to CD_3CN (400 μL). The nuclear magnetic resonance (NMR) reaction yield was determined by ^{1}H NMR based on the internal standard method using pyrazine as the standard substance. The isolated yield was calculated after the crude product being purified by chromatography over silica.

2.3. General procedure for cross-dehydrogenative reactions

2.3.1. Phosphonation of N-aryltetrahydroisoquinolines

A 5 mL flask was charged with methanol (0.5 mL), *N*-aryltetrahydroisoquinoline substrate (0.5 mmol), and photocatalyst (1 mol% based on monomer). The mixture was open to air in the flask and magnetically stirred at room temperature under irradiation of 23 W white LED lamp at a distance around 8 cm. The reaction was stopped by switching off the LED lamp after 24 h, and the photocatalyst was separated by centrifugation. The solvent was removed under vacuum, and the reaction yields were determined by ^{1}H NMR based on the internal standard method using pyrazine as the standard substance after dissolving the crude product in $CDCl_3$.

2.3.2. Aza-Henry reactions

A 5 mL flask was charged with nitromethane or nitroethane (1 mL), *N*-aryltetrahydroisoquinoline substrate (0.5 mmol), and photocatalyst (1 mol% based on monomer). The mixture was open to air in the flask and magnetically stirred at room temperature under irradiation of 23 W white LED lamp at a distance around 8 cm. The reaction was stopped by switching off the LED lamp after 24 h, and the photocatalyst was

separated by centrifugation. The supernatant was removed under vacuum. The reaction yields were determined by ^{1}H NMR based on the internal standard method using pyrazine as the standard substance after dissolving the crude product in $CDCl_3$ or d_6-dimethyl suloxide (d_6-DMSO).

2.4. General procedure for C-3 functionalization reaction of indoles

2.4.1. C-3 formylation of indoles

A 5 mL flask was charged with acetonitrile (5 mL), indole substrate (1 mmol), *N*,*N*,*N*',*N*'-tetramethylethylenediamine (TMEDA, 0.3 mL), H_2O (0.05 mL), KI (664 mg), and photocatalyst (4 mol% based on monomer). The mixture was open to air in the flask and magnetically stirred at room temperature under irradiation of 23 W white LED lamp at a distance around 8 cm. The reaction was stopped by switching off the LED lamp after 48 h, and the photocatalyst was separated by centrifugation. The supernatant was removed under vacuum. The reaction yields were determined by ^{1}H NMR based on the internal standard method using pyrazine as the standard substance after dissolving the crude product in $CDCl_3$ or d_6-DMSO.

2.4.2. C-3 thiocyanation of indoles

A 5 mL flask was charged with THF (5 mL), indole substrate (1 mmol), NH_4SCN (2 mmol), and photocatalyst (4 mol% based on monomer). The mixture was open to air in the flask and magnetically stirred at room temperature under irradiation of 23 W white LED lamp at a distance around 8 cm. The reaction was stopped by switching off the LED lamp after 48 h and the photocatalyst was separated by centrifugation. The supernatant was removed under vacuum. The reaction yields were determined by ^{1}H NMR based on the internal standard method using pyrazine as the standard substance after dissolving the crude product in $CDCl_3$ or d_6-DMSO.

3. Results and discussion

3.1. Synthesis and characterizations of sp^{2}C-COFs

The sp^{2}C-COFs were synthesized by Aldol reaction between TMT and TPA or TBPA at 180 °C for 3 days in Teflon-lined steel autoclave, named TPA-sp^{2}C-COF and TBPA-sp^{2}C-COF, respectively (Fig. 1). The chemical structures of TPA-sp^{2}C-COF and TBPA-sp^{2}C-COF were confirmed by Fourier transform infrared (FT-IR) spectroscopy and solid-state ^{13}C nuclear magnetic resonance (solid-state ^{13}C NMR) spectroscopy (Figs. S1 and S2). In the FT-IR spectra of TPA-sp^{2}C-COF and TBPA-sp^{2}C-COF, =the C=C stretching vibration bands at 1621 cm^{-1} appear, and =the C=O stretching vibration bands at 1680 cm^{-1} belonged to monomer TPA or TBPA decrease obviously. Notably, the presence =of *trans*-HC=CH- stretching vibration bands at 970 cm^{-1} confirms the *trans*-configurations of olefin linkages in the TPA-sp^{2}C-COF and TBPA-sp^{2}C-COF [26]. Meanwhile, the peaks at 170, 148, and 140 ppm in solid-state ^{13}C NMR spectra of TPA-sp^{2}C-COF and TBPA-sp^{2}C-COF are corresponded to the carbon atoms in triazine rings, N–C, =and C=C bonds, respectively [27]. The results of elemental analysis are in agreement approximately with the theoretical values, which also prove the successful preparation of TPA-sp^{2}C-COF and TBPA-sp^{2}C-COF (see the Supplementary Material).

The crystallinities of TPA-sp^{2}C-COF and TBPA-sp^{2}C-COF were examined by powder X-ray diffraction (PXRD) measurement. PXRD patterns show that the crystallinity of TBPA-sp^{2}C-COF is higher than that of TPA-sp^{2}C-COF, which is owing to the better molecular planarity of TBPA as compared with that of TPA. For TPA-sp^{2}C-COF, the PXRD peaks at 6.0°, 10.7°, 12.4°, 16.5°, and 20.0° can be assignable to the (100), (110), (200), (210), and (001) facets, respectively (Fig. 2a). The TBPA-sp^{2}C-COF exhibits PXRD peaks at 4.3°, 7.4°, 8.6°, 11.9°, and 22.4°, which are assigned to the (100), (110), (200), (210), and (001) facets, respectively (Fig. 2b). Structural models with eclipsed AA and staggered AB stacking were simulated for the sp^{2}C-COFs by Material

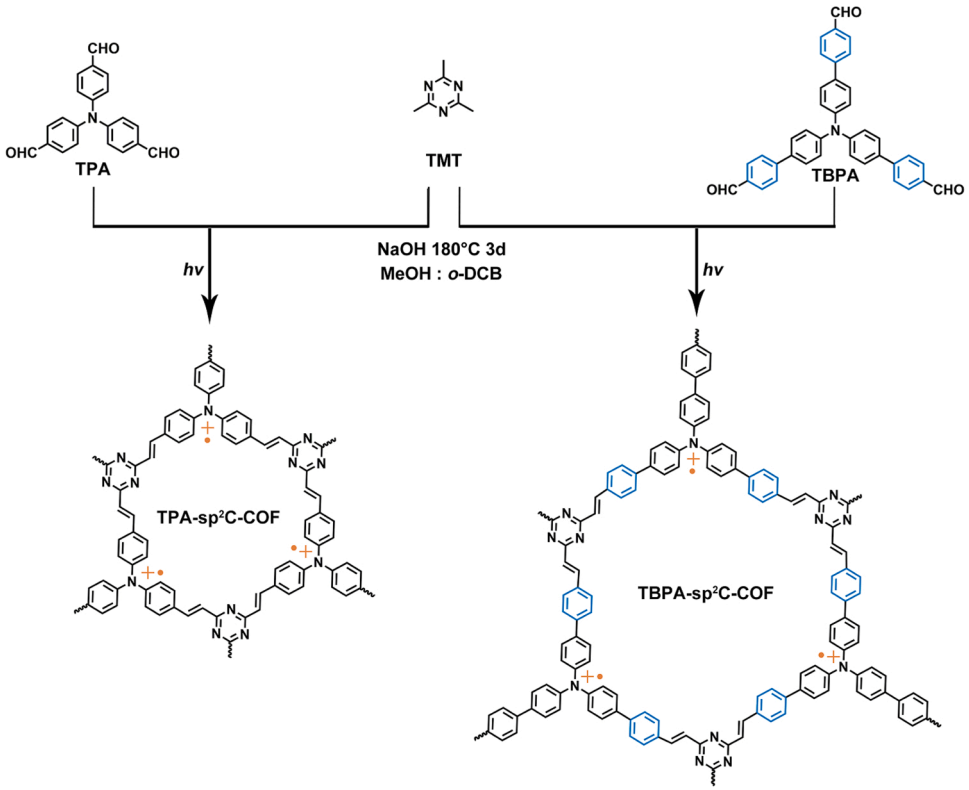

Fig. 1. Synthesis of persistent radical cation sp^{2}C-COFs by Aldol condensation reaction of TMT and TPA or TBPA.

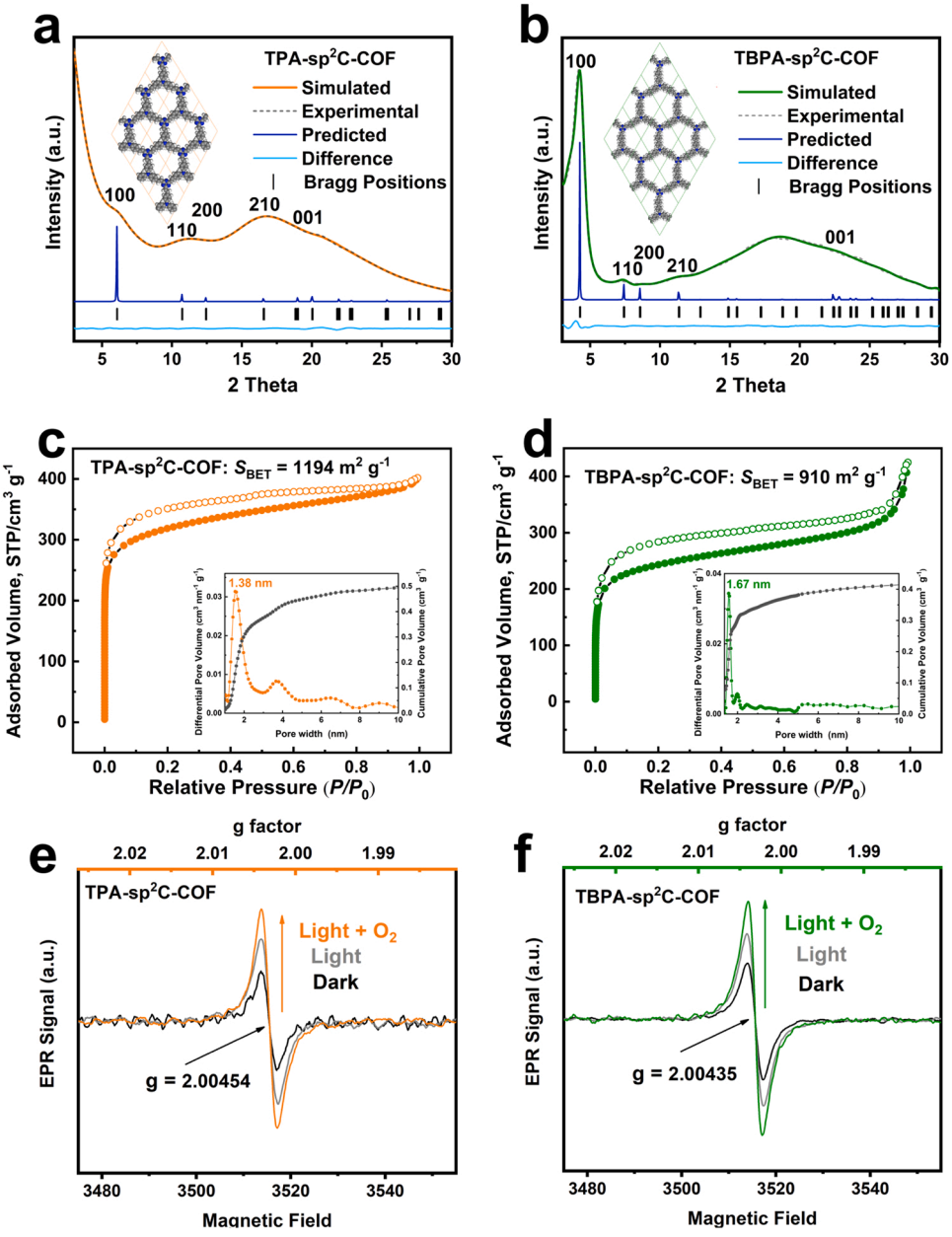

Fig. 2. PXRD patterns of (a) TPA-sp^{2}C-COF and (b) TBPA-sp^{2}C-COF with Rietveld refinement and corresponding molecular models (insets). Nitrogen sorption isotherms and pore size distributions calculated from non-local density functional theory (insets) of (c) TPA-sp^{2}C-COF and (d) TBPA-sp^{2}C-COF. The EPR spectra of solid-state samples of (e) TPA-sp^{2}C-COF and (f) TBPA-sp^{2}C-COF under dark, light irradiation, and light + oxygen atmosphere.

Studio (Figs. S3 and S4). Among various possible stacking modes, the eclipsed AA stacking mode in space group $P6_3/m$ matches well with PXRD pattern of TPA-sp^{2}C-COF (R_{wp} = 0.41%, R_P = 0.29%) with the unit cell parameters of $a = b = 16.3$ Å, $c = 4.3$ Å, $\alpha = \beta = 90°$, $\gamma = 120°$. In the case of TBPA-sp^{2}C-COF, the eclipsed AA stacking model in space group $P6_3/m$ matches well with the PXRD pattern (R_{wp} = 3.29%, R_P = 2.69%) with the cell parameter of $a = b = 23.8$ Å, $c = 3.5$ Å, $\alpha = \beta = 90°$, $\gamma = 120°$ (Tables S1 and S2). All the Rietveld refined PXRD patterns of TPA-sp^{2}C-COF and TBPA-sp^{2}C-COF match their experimentally observed curves with a negligible difference.

The porosities of TPA-sp^{2}C-COF and TBPA-sp^{2}C-COF were analyzed by the N_2 adsorption and desorption isotherms at 77 K (Fig. 2c and d). According to the International Union of Pure and Applied Chemistry classification, these adsorption–desorption curves are classified as type I isotherm, signifying the presence of micropores in the COFs [28]. The Brunauer–Emmett–Teller (BET) specific surface area values of TPA-sp^{2}C-COF and TBPA-sp^{2}C-COF are calculated to be 910 and 1190 m^2 g^{-1}, respectively (Fig. S5). Meanwhile, the pore size distribution profiles (insets in Fig. 2c and d) evaluated by the non-local density functional theory for TPA-sp^{2}C-COF (1.38 nm) and TBPA-sp^{2}C-COF (1.67 nm) are in conformity with the predicted pore diameters (1.43 and 1.85 nm), which are also in line with their stacking mode parameters.

The existence of photoinduced radical cation is directly confirmed by EPR measurements. The g factor calculated from EPR measurement reflects the characteristics of unpaired electrons, which can identify the types of radicals in the materials. The solid powders of TPA-sp^{2}C-COF and TBPA-sp^{2}C-COF exhibit strong resonance signals at $g = 2.00454$ and 2.00435, which are assigned to $TPA^{+\bullet}$ in the skeleton coming from the p^5 orbital splitting in N atom in TPA-sp^{2}C-COF and TBPA-sp^{2}C-COF (Fig. 2e and f) [29,30]. The EPR test data of $TPA^{+\bullet}$ show that the radical cation can be quenched using ethanol as quencher, and the signal can return to the previous level after the removal of ethanol (Fig. S6). The radical

cation amount will be further enhanced (from 6.8% to 10.7% for TBPA-sp^{2}C-COF and from 1.6% to 2.9% for TPA-sp^{2}C-COF) when these materials are exposed to xenon lamp source (Microsolar 300, from Beijing perfectlight) rather than the dark environment, which suggests that the radical cations can be formed by light excitation. In addition, in the presence of oxygen, the amount of $TPA^{+\bullet}$ will be further improved (13.2% for TBPA-sp^{2}C-COF and 3.58% for TPA-sp^{2}C-COF), which is in line with our previous speculation that the sp^{2}C-COF materials can generate $TPA^{+\bullet}$ and $O_2^{-\bullet}$ in the presence of light and oxygen. The process is demonstrated as follows, TPA $+ h\nu \rightarrow$ TPA* $+ O_2 \rightarrow TPA^{+\bullet} + O_2^{-\bullet}$. Although the radical yield has a big gap between the chemical initiation radicals (about 10–60%) and photogenerated radicals (maximum 13.2% in this paper), we believe that this green and pollution-free initiation method possesses a great development prospect [31]. In addition, X-ray photoelectron spectroscopy (XPS) were conducted to further confirm the existence of $TPA^{+\bullet}$ radical cations. The N 1s spectra can be divided into three peaks, and the signal at 400.9 eV is assigned to the N in $TPA^{+\bullet}$ (Fig. S7) [32].

3.2. Optical and electronic properties of sp^{2}C-COFs

The electronic properties of these sp^{2}C-COFs were systematically investigated by electrochemical measurements, photo-physical measurements, and density function theory (DFT) calculations. DFT calculations were performed on molecular models of sp^{2}C-COFs using Dmol3 module in Material Studio software (Fig. 3). In TPA-sp^{2}C-COF, the highest occupied molecular orbital (HOMO) is located at the TPA fragment and the C=C bridge, and the lowest unoccupied molecular orbital (LUMO) is located at the triazine ring, =C=C bridge, and the benzene ring [33]. This D–A structure allows electrons to be transferred under light irradiation from the TPA unit to the triazine ring through the PET process. Therefore, the TPA unit loses an electron that can be trapped by oxygen molecules, and the persistent $TPA^{+\bullet}$ is left in the skeleton structure of TPA-sp^{2}C-COF. Furthermore, the rigid COF skeleton keeps the radical cations apart, preventing them from reacting with each other. Notably, as compared with the electronic structure of TPA-sp^{2}C-COF, the HOMO and the LUMO in the TBPA-sp^{2}C-COF are more independent on skeleton, that is, the overlap degree is smaller. This separated D–A structure coincides with an effective intramolecular energy transfer strategy named TBET that requires an electronically conjugated bridge to link the donor and acceptor in a noncoplanar manner [34]. Therefore, the TBPA-sp^{2}C-COF and TPA-sp^{2}C-COF should show different properties in lifetime of excited state, charge separation, charge recombination, *etc.*, which will be confirmed by several characterizations as follows.

To confirm the above speculation, the band structure and excited state properties of the two materials are examined firstly. Mott–Schottky (M–S) plot (Figs. 4a and S8), UV–vis diffuse reflection spectroscopy (UV–vis DRS) (Fig. 4b), Tauc plot (Fig. S9), and ultraviolet photoelectron spectroscopy (UPS) (Fig. 4c and d) were implemented to study the energy level of valence band maximum (E_{VB}) band and conduction band minimum (E_{CB}) of TPA-sp^{2}C-COF and TBPA-sp^{2}C-COF [35]. Both M–S plots of TPA-sp^{2}C-COF and TBPA-sp^{2}C-COF exhibit positive slopes, which suggest their n-type semiconductor behaviors, and the flat band potentials of TPA-sp^{2}C-COF and TBPA-sp^{2}C-COF are calculated to be –1.90 and −2.07 V vs. normal hydrogen electrode (NHE) at pH = 7, respectively. In general, the flat band position is close to the E_{CB} in n-type semiconductor, hence the flat band potential is used as the E_{CB} value in this paper [26]. The E_{CB} values of these two sp^{2}C-COFs are so negative that no similar example has been reported among COFs and other porous organic polymers, indicating that these sp^{2}C-COFs possess excellent reducibility for their photogenerated electrons with high activity [36]. The TPA-sp^{2}C-COF and TBPA-sp^{2}C-COF show broad visible absorption ranges in UV–vis DRS up to 600 and 550 nm, respectively, and their band gaps are estimated to be 1.99 and 2.01 eV from Tauc plots, respectively [37]. It is worth nothing that the peak at 690 nm assigned to the $TPA^{+\bullet}$ confirmed the existence of radical cations (Fig. 4b). The E_{VB} result is 0.09 and −0.06 eV for TPA-sp^{2}C-COF and TBPA-sp^{2}C-COF, respectively, which is determined by the E_{CB} and the band gap (Fig. 4e). These values are similar to the UPS results (–4.93 eV

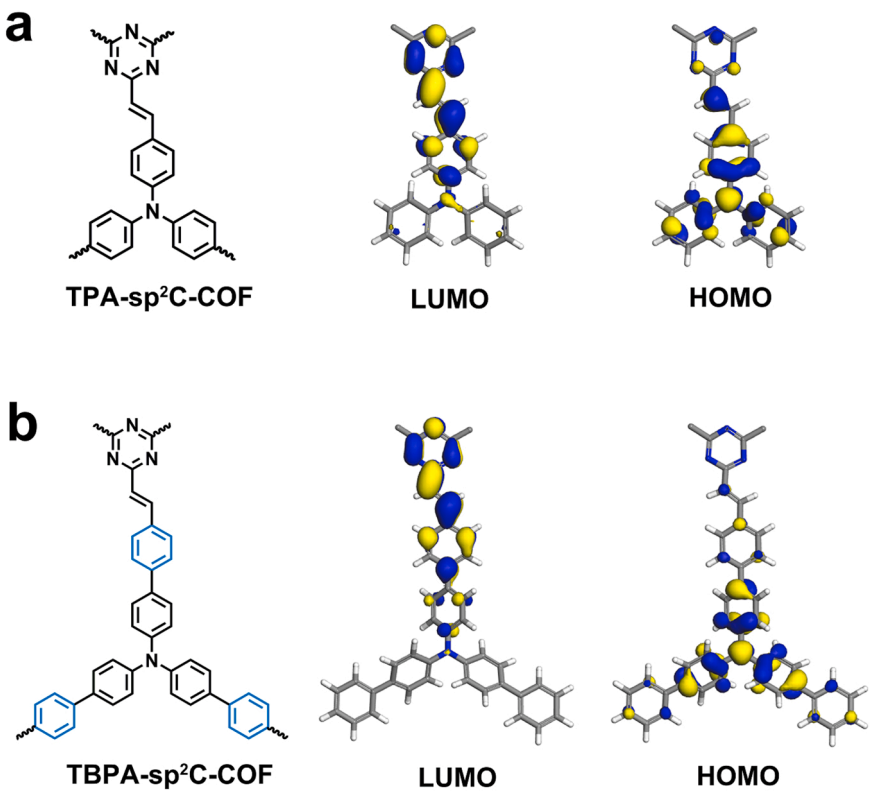

Fig. 3. The HOMO and LUMO of molecular models of TPA-sp^{2}C-COF (a) and TBPA-sp^{2}C-COF (b) calculated by DFT.

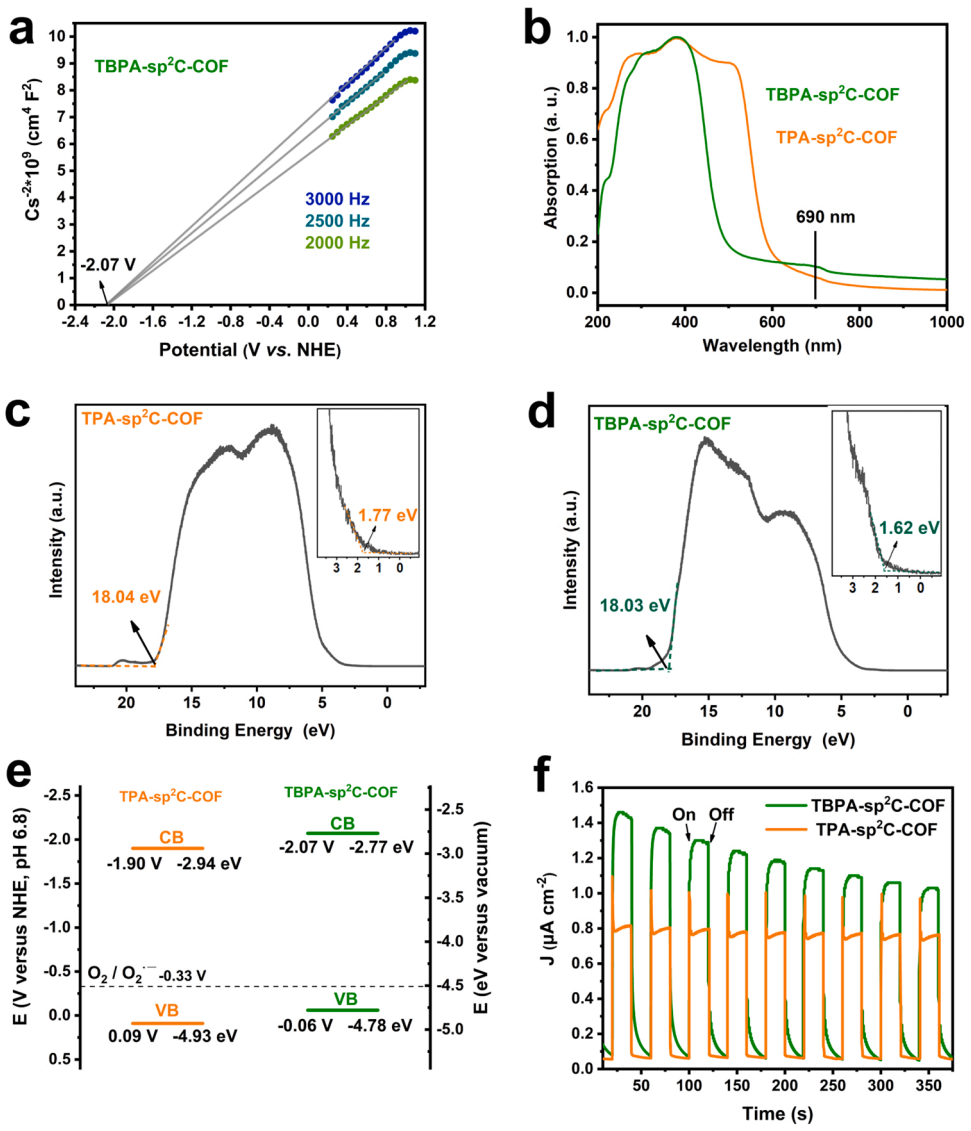

Fig. 4. (a) Mott–Schottky plots of TBPA-sp^{2}C-COF. (b) Steady state absorption spectra of TPA-sp^{2}C-COF (orange) and TBPA-sp^{2}C-COF (green). UPS spectra of (c) TPA-sp^{2}C-COF and (d) TBPA-sp^{2}C-COF. (e) The band energy diagrams and (f) photocurrent response curves of TPA-sp^{2}C-COF (orange) and TBPA-sp^{2}C-COF (green).

for TPA-sp^{2}C-COF and −4.79 eV for TBPA-sp^{2}C-COF vs. vacuum level), which is calculated by subtracting the UPS width from excitation energy (He-I, 21.22 eV). The properties of the excited state were preliminarily explored by time-resolved fluorescent decay spectroscopy (TRFDS). The decay curves of TBPA-sp^{2}C-COF and TPA-sp^{2}C-COF fit the data form the test and the average lifetime is estimated to be 2.65 (TBPA-sp^{2}C-COF) and 0.457 ns (TPA-sp^{2}C-COF) under the setup of optimal excitation and emission wavelength (Figs. S10 and S11). The longer lifetimes of excited state in TBPA-sp^{2}C-COF reveal that its photogenerated charges are more likely to be used for catalytic reactions as compared with TPA-sp^{2}C-COF [38]. From the view of material structure, TBPA-sp^{2}C-COF possesses one more benzene ring than TPA-sp^{2}C-COF between the donor and the acceptor in the sp^{2}C-COF repeat unit thus the effective TBET system are formed in skeleton. We believe that the barrier effect of benzene ring greatly prolongs the time of charge recombination, so that the material presents excited state with a long lifetime. Transient photocurrent responses further illustrate the difference in charge separation and charge recombination processes between TBPA-sp^{2}C-COF and TPA-sp^{2}C-COF, while the charge transfer capacities of these sp^{2}C-COFs are similar as shown in electrochemical impedance spectroscopy test (Figs. 4f and S12). Under the light irradiation, the photocurrent signal of TPA-sp^{2}C-COF appears instantaneously, while the signal of TBPA-sp^{2}C-COF slowly reaches its platform value. This phenomenon indicates that the TBPA-sp^{2}C-COF has slower charge separation rate than that of TPA-sp^{2}C-COF. Similarly, the fast decline of photocurrent in TPA-sp^{2}C-COF reveals that it has a faster charge recombination rate than that of TBPA-sp^{2}C-COF when the xenon lamp is turned off. Therefore, these data well confirm that the existence of TBET system can reduce the charge separation and charge recombination rates of COFs. Furthermore, TBPA-sp^{2}C-COF with relatively slow charge separation and charge recombination rate exhibits a significantly larger photocurrent signal than that of TPA-sp^{2}C-COF, indicating that the effect of charge recombination rate on the lifetime of the excited state is much greater than that of charge separation rate due to the contribution of charge recombination to photocurrent signal is more than the negative effect caused by charge separation.

In order to get detailed information about the excited state of TPA-sp^{2}C-COF and TBPA-sp^{2}C-COF under light irradiation, the fs-TA spectroscopy measurements were performed following 400 nm excitation. The fs-TA spectra of TPA-sp^{2}C-COF and TBPA-sp^{2}C-COF (Fig. 5a–d) show negative features at 465 and 475 nm due to ground state bleaching process, which also corresponds to the steady state absorption spectra of

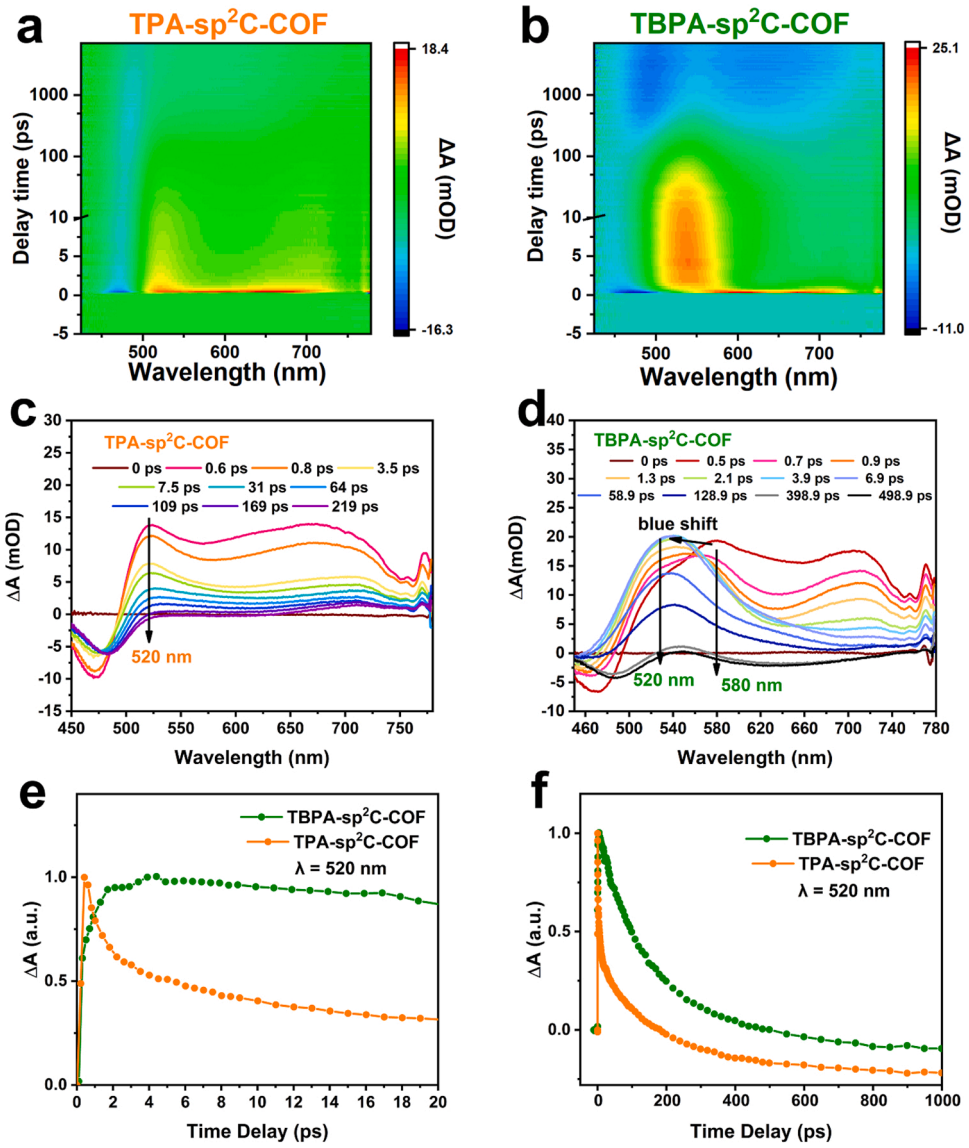

Fig. 5. The fs-TA spectra of (a) TPA-sp^{2}C-COF and (b) TBPA-sp^{2}C-COF following 400 nm excitation. The spectra of (c) TPA-sp^{2}C-COF and (d) TBPA-sp^{2}C-COF at pump-probe time delays chosen to highlight the changing nature of the excited electronic states. Comparison of kinetics of TPA-sp^{2}C-COF (orange) and TBPA-sp^{2}C-COF (green) at 520 nm on different time scales of (e) 20 and (f) 1000 ps.

the materials (Fig. 4b) [39]. Both materials show positive signals from 480 to 750 nm, and the maximum value is demonstrated at 520 nm. This signal can be assigned to the absorption derived from PET, and directly shows the process of charge separation and charge recombination within the two materials under light irradiation [40]. The TPA-sp^{2}C-COF signal reaches its maximum value at about 0.6 ps at 520 nm, while the TBPA-sp^{2}C-COF signal reaches its maximum value at about 4 ps at 520 nm (Fig. 5c and 5d), suggesting that TBPA-sp^{2}C-COF has a slower charge separation rate as compared with that of TPA-sp^{2}C-COF owing to the barrier effect of benzene ring in the skeleton. It is worth noting that the signal at 580 nm in TBPA-sp^{2}C-COF reaches its maximum value at 0.5 ps, which is consistent with the charge separation rate of TPA-sp^{2}C-COF. However, the peak at 580 nm weakens rapidly around 1.0 ps and a new peak appears at 520 nm, which means that the interaction between the photogenerated electrons and holes has changed (Fig. 5e). From the view of chemical structure, the phenomenon of the blue-shift just shows that the large dipole is formed during the photogenerated electron transfer from donor unit (triphenylamine) to accepter unit (triazine ring) by crossing benzene ring in TBPA-sp^{2}C-COF. This is also due to the presence of lower energy electron states originated from precise structural design in the TBPA-sp^{2}C-COF than in the TPA-sp^{2}C-COF, which assists the separation of the electrons and holes [41,42]. Surprisingly, the barrier effect of benzene ring directly leads to the significantly lower charge recombination rate of TBPA-sp^{2}C-COF than that of TPA-sp^{2}C-COF, for the charge recombination time of TBPA-sp^{2}C-COF and TPA-sp^{2}C-COF is about 500 and 170 ps at 520 nm, respectively (Fig. 5f). In summary, the PET processes of those materials are further clarified, and the electrons from triphenylamine are transferred to triazine ring to form $TPA^{+\bullet}$ and highly reactive electrons. Notably, the lifetime of the excited state is doubled owing to the formation of TBET system, which provides a new avenue to regulate the excited state lifetime of the material.

3.3. Photocatalytic studies

Considering that the two sp^{2}C-COFs possess long lifetime of excited state and extremely negative reduction potential, they were utilized as photocatalysts in oxidative hydroxylation of aryl boronic acids into phenols under light irradiation (Fig. 6). Phenolic compounds as the reaction products are intermediates of many biologically active

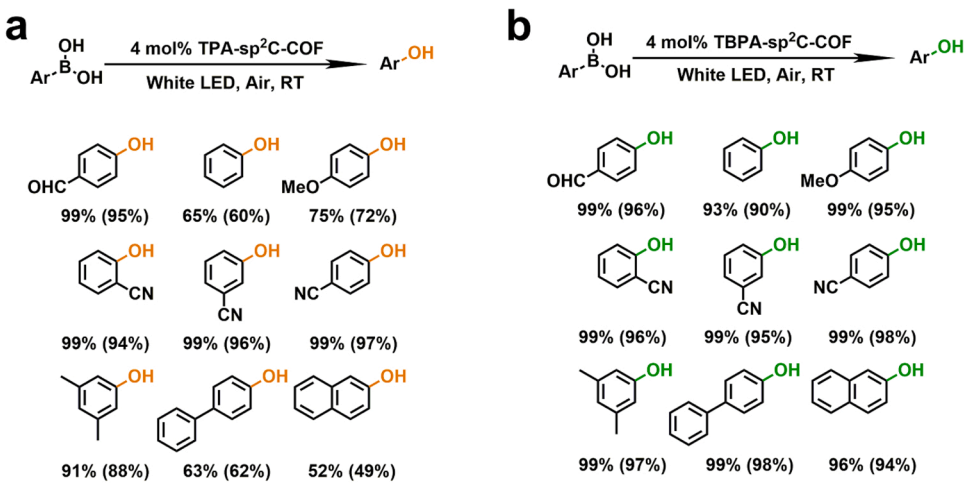

Fig. 6. Heterogeneous photocatalytic oxidative hydroxylation of aryl boronic acids. Reaction conditions: aryl boronic acids (0.5 mmol), dimethyl formamide (5 mL), (a) TPA-sp^{2}C-COF or (b) TBPA-sp^{2}C-COF (4 mol% based on monomer), and 23 W white LED bulb at a distance around 8 cm. Yield was determined by ^{1}H NMR using pyrazine as the standard substance (internal standard method). The isolated yield (in the brackets) was calculated after the crude product being purified by chromatography over silica.

components and organic synthesis [43]. Therefore, considerable researches have been devoted to obtaining phenolic compounds in a green and economical reaction route. However, many catalytic systems reported are complex and uneconomical by introducing metals [44], oxygen atmospheres [45], high energy light sources [46], and in particular, cocatalysts. The commonly used cocatalyst such as triethylamine can greatly promote the progress of photocatalytic reaction, but its toxicity can cause great pollution to the environment. So far, this reaction cannot carry out without the help of a cocatalyst in any heterogeneous catalytic systems. Here, TPA-sp^{2}C-COF and TBPA-sp^{2}C-COF are used as photocatalysts to catalyze such reactions in a totally green reaction system that is cocatalyst-free, metal-free, and under mild condition (at room temperature and in air atmosphere). The catalysis reactions were performed using air as oxidizing agent and DMF as solvent. Besides the sp^{2}C-COF as catalyst and substrates, no cocatalyst is added to this catalytic system. As shown in Fig. 6a, TPA-sp^{2}C-COF shows good catalytic activity with the yields up to 99% for oxidative hydroxylation of aromatic boric acid with electron-withdrawing substituents such as CN or CHO on the aromatic ring. However, the catalytic activity of TPA-sp^{2}C-COF is not good for those aromatic groups with electron-donating or obvious conjugation effect substituents. But for TBPA-sp^{2}C-COF, almost all of the substrates were quantitatively depleted and transformed into the corresponding phenols and the yields determined by ^{1}H NMR can reach 93–99%, while the isolated yields can reach 90–98% in Fig. 6b. TBPA-sp^{2}C-COF possesses good applicability for aryl boric acid with various functional groups, and its catalytic activity is higher than that of TPA-sp^{2}C-COF owing to the high density of photogenerated charges coming from slow charge recombination process. Interestingly, this is the first report of heterogeneous photocatalysts that can successfully catalyze the oxidation of phenylboric acid in air, at room temperature, and without any assistance of cocatalysts and metals. The two sp^{2}C-COF catalysts show good cycling stability, and there are no noticeable decays in catalytic activity in the first three cycles (Fig. S13). Even after ten cycles, these catalysts retain about 80% of activity without dramatic decline in catalytic performance, and the chemical structure, crystal nature, and porosity of these two sp^{2}C-COFs are still maintained based on the analysis of FT-IR, PXRD, and nitrogen sorption isotherm measurements (Figs. S14–S16). To test the wavelength dependence of the photocatalytic performance, the yields of this reaction catalyzed by TBPA-sp^{2}C-COF were measured with the long-wavelength pass filters (LPF) (Fig. S17). The catalytic yield is about 80% under light irradiation at the wavelength greater than 420 nm, indicating that the material possesses excellent catalytic efficiency in the visible region. The apparent quantum yields (AQY) of the reaction are wavelength dependent (Fig. S18), and show the maximum of 5.3% and 6.6% at 380 nm for TPA-sp^{2}C-COF and TBPA-sp^{2}C-COF, respectively. As compared with other catalysts for this catalytic reaction reported in recent years, these two sp^{2}C-COFs exhibit excellent catalytic performance under milder catalytic conditions (Table S3).

Based on the physical properties and excellent catalytic performance of these sp^{2}C-COFs, a hypothetical catalytic mechanism is proposed (Fig. 7a). Under the excitation of visible light, the electrons from the electron donor unit (triphenylamine) are transferred to the electron acceptor unit (triazine ring) through the PET process, generating persistent $TPA^{+\bullet}$ and highly active electrons. The CB positions of these sp^{2}C-COFs are more negative than the potential required for the reduction of O_2 to superoxide radical anions ($O_2^{-\bullet}$), hence the O_2 in the air quenches the photogenerated electrons and then produces $O_2^{-\bullet}$. The EPR spectra can confirm the presence of superoxide anionic radicals in both sp^{2}C-COFs (Figs. 7b and S19) [47]. The sharp twelve-fold peak matches the typical signal of $O_2^{-\bullet}$ under xenon lamp irradiation. In the process of the catalysis, the $O_2^{-\bullet}$ attacks the boric acid group, and then goes through a series of rearrangement and elimination reactions to produce phenol-based products [48]. Both sp^{2}C-COFs cannot produce other kinds of ROS species such as hydroxyl radicals (Fig. S20). In addition, the control experiment also proves that the light, air, and catalyst are essential conditions for this catalytic reaction. No product is detected in the nitrogen atmosphere, suggesting that the reaction could not take place without oxygen. When the $O_2^{-\bullet}$ scavenger is added to the catalytic system, the reaction yield decreases significantly (8%). But when the •OH scavenger or $^1O_2$ scavenger is introduced in the catalytic system, the reaction yield shows no significant loss. These results confirm that the $O_2^{-\bullet}$ is the only ROS existing in the system, and this conclusion is consistent with that of the EPR experiments. To further clarify whether electrons or holes determine this process ($TPA + h\nu \rightarrow TPA^* + O_2 \rightarrow TPA^{+\bullet} + O_2^{-\bullet}$), the quenching experiments of electron and hole were also performed. When the electron scavenger is added into the reaction system, the reaction yield was reduced to 19%. In the meanwhile, the reaction yield remains at 91% in the presence of hole scavenger. These experimental results reveal that electron and $O_2^{-\bullet}$ are the key active species that play a major role during substrate conversion (Table S4).

Since these sp^{2}C-COFs show excellent catalytic efficiency for the oxidation of phenylboric acid, we chose TBPA-sp^{2}C-COF to test the versatility of other photocatalytic oxidative organic transformations, such as photocatalytic cross-dehydrogenative coupling (CDC) reaction (Fig. 8a) and the C-3 functionalization reaction of indoles (Fig. 8b). CDC reaction can directly convert C–H into C–C or C–P bonds, which is a powerful tool for the synthesis of natural products [49]. 3-Substituted indoles are also important intermediates that have been widely used in agrochemicals and pharmaceutical drug fields [50]. Notably, both of these reactions require the catalyst to provide highly active electrons.

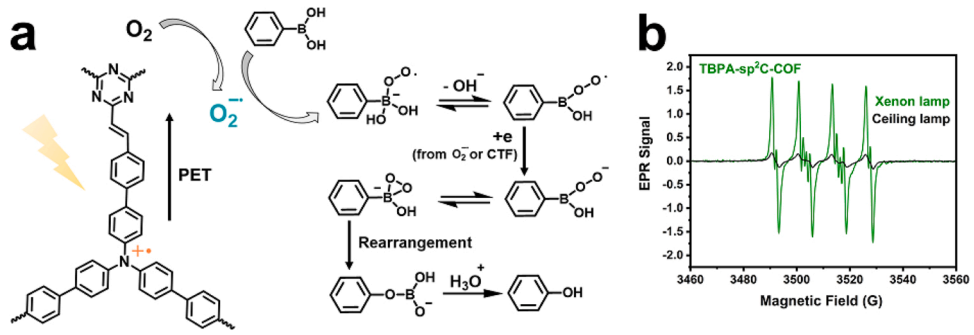

Fig. 7. (a) The proposed catalytic mechanism of photocatalytic oxidative hydroxylation of aryl boronic acids without the assistance of cocatalyst. (b) The detection of $O_2^{-\bullet}$ in a mixture of 5,5-dimethyl-1-pyrroline-1-oxide and TBPA-sp^{2}C-COF in acetonitrile under ceiling lamp or xenon lamp irradiation using EPR spectra.

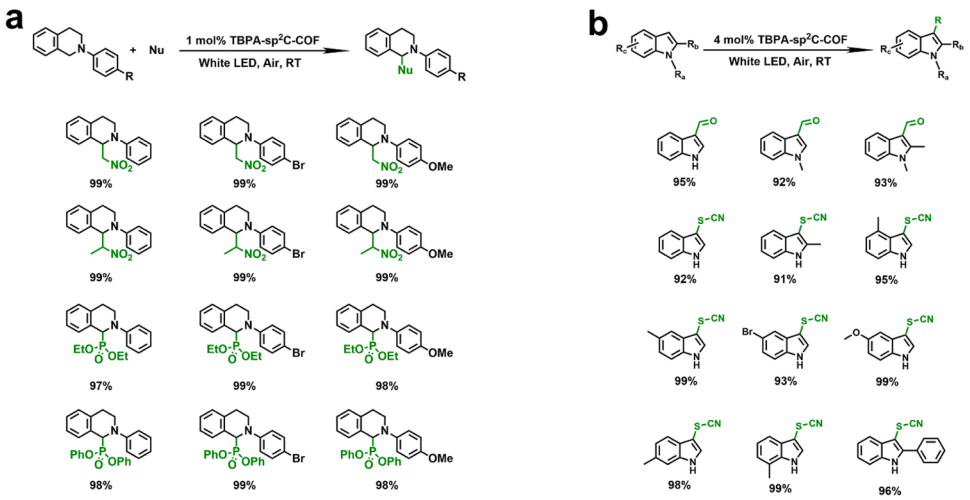

Fig. 8. (a) Photocatalytic cross-dehydrogenative coupling reactions catalyzed by TBPA-sp^{2}C-COF. Reaction conditions for phosphonylation of amine: *N*-aryltetrahydroisoquinolines (0.5 mmol), phosphite ester (0.5 mmol), TBPA-sp^{2}C-COF (1 mol% based on monomer), methanol (0.5 mL), air, 24 h, 23 W white LED, room temperature. Aza-Henry reaction was conducted under similar conditions except 1 mL of nitromethane or nitroethane was used instead of phosphite ester and MeOH. (b) C-3 functionalization reaction of indole catalyzed by TBPA-sp^{2}C-COF. Reaction conditions for C-3 formylation of indole: indole (0.5 mmol), *N*,*N*,*N*',*N*'-tetramethylethane-1,2-diamine (1 mmol), potassium iodide (2 mmol), TBPA-sp^{2}C-COF (4 mol% based on monomer), acetonitrile (5 mL), H_2O (50 μL), air, 48 h, 23 W white LED, room temperature. Reaction conditions for C-3 thiocyanation of indole: indole (0.5 mmol), ammonium thiocyanate (1 mmol), TBPA-sp^{2}C-COF (4 mol% based on monomer), tetrahydrofuran (5 mL), air, 48 h, 23 W white LED, room temperature. All the yields were determined by ^{1}H NMR using pyrazine as the internal standard substance.

For CDC reaction, several substrates were converted smoothly in both aza-Henry reaction and phosphonation reaction under light irradiation. Four nucleophiles (nitroalkanes and phosphite esters) can react with three substituted *N*-aryltetrahydroisoquinoline in the presence of catalyst TBPA-sp^{2}C-COF with a great yield (97–99%). For the C-3 functionalization of indole, the formyl substitution and thiocyanide substitution of 3-substituted indoles can be carried out smoothly with high catalytic efficiency (yield determined by ^{1}H NMR: 91–99%). Interestingly, this is the first report of successfully heterogeneous catalysis of C-3 functionalization of indoles in air rather than in oxygen atmosphere. This result also indicates that the highly reactive electrons produced by the TBPA-sp^{2}C-COF can be used to generate ROS with a great efficiency to catalyze various reactions.

4. Conclusions

We successfully prepared two sp^{2}C-COFs containing persistent radical cation (TPA$^{+\bullet}$). This kind of radical cation originates from the unpaired electrons on the N atom in the TPA and TBPA units, which are delocalized through the PET process owing to the effective D–A heterojunction to form high energy photogenerated electrons and TPA$^{+\bullet}$. The photogenerated electrons can be gradually consumed by O_2 to form $O_2^{-\bullet}$, leaving more radical cations in the skeleton of these sp^{2}C-COFs. Therefore, enhanced signal of TPA$^{+\bullet}$ can be detected in the EPR under the light irradiation. Meanwhile, we use the fs-TA spectra to accurately illustrate the successful construction of TBET system in TBPA-sp^{2}C-COF, which can greatly reduce the charge recombination rate so as to further improve the lifetime of excited state and catalytic efficiency. These materials with high energy photogenerated electrons can be used for visible light catalyzing oxidative hydroxylation of aryl boronic acids into phenols in a totally green procedure. Notably, this is the first example of photocatalyst to successfully realizing this reaction in air, at room temperature, and without any assistance of cocatalysts and metals. Owing to long lifetime of excited state and large conjugated structure between these two sp^{2}C-COFs, the TBPA-sp^{2}C-COF with effective ROS activity exhibits excellent catalytic performance in oxidative hydroxylation of aryl boronic acids reactions, CDC reaction, and C-3 functionalization of indole. This work explored the possibility of forming photoinduced radical cations in COFs for the first time and successfully obtaining two kinds of PIR-COFs. In addition, the conclusion of these materials with high performance in heterogeneous photocatalysis is also confirmed. We believe that this work will bring new ideas to both the radical chemistry fields and COF fields, and will deepen the integration of the two fields thus develop a range of new materials with interesting properties.

CRediT authorship contribution statement

Yuan-Zhe Cheng: Conceptualization, Investigation, Validation, Writing – original draft. **Wenyan Ji:** Conceptualization, Methodology, Investigation, Writing – original draft. **Xianxin Wu:** Validation, Data curation. **Xuesong Ding:** Conceptualization, Writing – review & editing,

Supervision. **Xin-Feng Liu:** Formal analysis, Data curation. **Bao-Hang Han:** Writing – review & editing, Supervision, Project administration, Funding acquisition.

Author contributions

X.D. and **B.-H.H.** designed the project. **Y.-Z.C.** prepared the sp^2C-COFs and measured the structure, composition and photocatalytic performances of the materials. **W.J.** and **Y.-Z.C.** contributed to the photophysical properties test and analysis. **X.W.** and **X.-F.L.** conducted the fs-TA experiments and analysis. **Y.-Z.C.**, **W.J.**, **X.W.**, **X.D.**, **X.-F.L.** and **B.-H.H.** co-wrote the paper. All the authors discussed the results and commented on the manuscript.

Declaration of Competing Interest

The authors declare that they have no known competing financial interests or personal relationships that could have appeared to influence the work reported in this paper.

Acknowledgements

The financial support of the National Natural Science Foundation of China (Grants 22075060, 21911530146, and 12074086) and the Strategic Priority Research Program of Chinese Academy of Sciences (Grant XDB36000000) is acknowledged.

Appendix A. Supporting information

Supplementary data associated with this article can be found in the online version at doi:10.1016/j.apcatb.2022.121110.

References

[1] K. Geng, T. He, R. Liu, S. Dalapati, K.T. Tan, Z. Li, S. Tao, Y. Gong, Q. Jiang, D. Jiang, Covalent organic frameworks: design, synthesis, and functions, Chem. Rev. 120 (2020) 8814–8933, https://doi.org/10.1021/acs.chemrev.9b00550.

[2] A. Wilson, G. Gasparini, S. Matile, Functional systems with orthogonal dynamic covalent bonds, Chem. Soc. Rev. 43 (2014) 1948–1962, https://doi.org/10.1039/C3CS60342C.

[3] E. Jin, J. Li, K. Geng, Q. Jiang, H. Xu, Q. Xu, D. Jiang, Designed synthesis of stable light-emitting two-dimensional sp^2carbon-conjugated covalent organic frameworks, Nat. Commun. 9 (2018) 4143, https://doi.org/10.1038/s41467-018-06719-8.

[4] E. Jin, M. Asada, Q. Xu, S. Dalapati, M.A. Addicoat, M.A. Brady, H. Xu, T. Nakamura, T. Heine, Q. Chen, D. Jiang, Two-dimensional sp^2 carbon–conjugated covalent organic frameworks, Science 357 (2017) 673–676, https://doi.org/10.1126/science.aan0202.

[5] S. Bi, C. Yang, W. Zhang, J. Xu, L. Liu, D. Wu, X. Wang, Y. Han, Q. Liang, F. Zhang, Two-dimensional semiconducting covalent organic frameworks via condensation at arylmethyl carbon atoms, Nat. Commun. 10 (2019) 2467, https://doi.org/10.1038/s41467-019-10504-6.

[6] A. Acharjya, P. Pachfule, J. Roeser, F.-J. Schmitt, A. Thomas, Vinylene-linked covalent organic frameworks by base-catalyzed aldol condensation, Angew. Chem. Int. Ed. 58 (2019) 14865–14870, https://doi.org/10.1002/anie.201905886.

[7] T. Jadhav, Y. Fang, W. Patterson, C.-H. Liu, E. Hamzehpoor, D.F. Perepichka, 2D poly(arylene vinylene) covalent organic frameworks via aldol condensation of trimethyltriazine, Angew. Chem., Int. Ed. 58 (2019) 13753–13757, https://doi.org/10.1002/anie.201906976.

[8] Y. Xiang, W. Dong, P. Wang, S. Wang, X. Ding, F. Ichihara, Z. Wang, Y. Wada, S. Jin, Y. Weng, H. Chen, J. Ye, Constructing electron delocalization channels in covalent organic frameworks powering CO_2 photoreduction in water, Appl. Catal. B Environ. 274 (2020), 119096, https://doi.org/10.1016/j.apcatb.2020.119096.

[9] C. Yuan, S. Fu, K. Yang, B. Hou, Y. Liu, L. Jiang, Y. Cui, Crystalline C–C and C=C bond-linked chiral covalent organic frameworks, J. Am. Chem. Soc. 143 (2021) 369–381, https://doi.org/10.1021/jacs.0c11050.

[10] S. Xu, H. Sun, M. Addicoat, B.P. Biswal, F. He, S. Park, S. Paasch, T. Zhang, W. Sheng, E. Brunner, Y. Hou, M. Richter, X. Feng, Thiophene-bridged donor-acceptor sp^2-carbon-linked 2D conjugated polymers as photocathodes for water reduction, Adv. Mater. 33 (2021), 2006274, https://doi.org/10.1002/adma.202006274.

[11] H. Lyu, C.S. Diercks, C. Zhu, O.M. Yaghi, Porous crystalline olefin-linked covalent organic frameworks, J. Am. Chem. Soc. 141 (2019) 6848–6852, https://doi.org/10.1021/jacs.9b02848.

[12] R. Chen, J.-L. Shi, Y. Ma, G. Lin, X. Lang, C. Wang, Designed synthesis of a 2D porphyrin-based sp^2carbon-conjugated covalent organic framework for heterogeneous photocatalysis, Angew. Chem., Int. Ed. 58 (2019) 6430–6434, https://doi.org/10.1002/anie.201902543.

[13] X. Huang, C. Sun, X. Feng, Crystallinity and stability of covalent organic frameworks, Sci. China Chem. 63 (2020) 1367–1390, https://doi.org/10.1007/s11426-020-9836-x.

[14] J.-L. Shi, R. Chen, H. Hao, C. Wang, X. Lang, 2D sp^2 carbon-conjugated porphyrin covalent organic framework for cooperative photocatalysis with tempo, Angew. Chem. Int. Ed. 59 (2020) 9088–9093, https://doi.org/10.1002/anie.202000723.

[15] S. Wei, F. Zhang, W. Zhang, P. Qiang, K. Yu, X. Fu, D. Wu, S. Bi, F. Zhang, Semiconducting 2D triazine-cored covalent organic frameworks with unsubstituted olefin linkages, J. Am. Chem. Soc. 141 (2019) 14272–14279, https://doi.org/10.1021/jacs.9b06219.

[16] H. Yu, D. Wang, Metal-free magnetism in chemically doped covalent organic frameworks, J. Am. Chem. Soc. 142 (2020) 11013–11021, https://doi.org/10.1021/jacs.0c02254.

[17] Z.X. Chen, Y. Li, F. Huang, Persistent and stable organic radicals: design, synthesis, and applications, Chem 7 (2021) 288–332, https://doi.org/10.1016/j.chempr.2020.09.024.

[18] F. Xu, H. Xu, X. Chen, D. Wu, Y. Wu, H. Liu, C. Gu, R. Fu, D. Jiang, Radical covalent organic frameworks: a general strategy to immobilize open-accessible polyradicals for high-performance capacitive energy storage, Angew. Chem. Int. Ed. 54 (2015) 6918–6922, https://doi.org/10.1002/anie.201501706.

[19] W. Cao, W.D. Wang, H.-S. Xu, I.V. Sergeyev, J. Struppe, X. Wang, F. Mentink-Vigire, Z. Gan, M.-X. Xiao, L.-Y. Wang, G.-P. Chen, S.-Y. Ding, S. Bai, W. Wang, Exploring applications of covalent organic frameworks: homogeneous reticulation of radicals for dynamic nuclear polarization, J. Am. Chem. Soc. 140 (2020) 6969–6977, https://doi.org/10.1021/jacs.8b02839.

[20] S.-L. Cai, Y.-B. Zhang, A.B. Pun, B. He, B.J. Yang, F.M. Toma, I.D. Sharp, O. M. Yaghi, J. Fan, S.-R. Zheng, W.-G. Zhang, Y. Liu, Tunable electrical conductivity in oriented thin films of tetrathiafulvalene-based covalent organic framework, Chem. Sci. 5 (2014) 4693–4700, https://doi.org/10.1039/c4sc02593h.

[21] Z. Mi, P. Yang, R. Wang, J. Unruangsri, W. Yang, C. Wang, J. Guo, Stable radical cations-containing covalent organic frameworks exhibiting remarkable structure-enhanced photothermal conversion, J. Am. Chem. Soc. 141 (2019) 14433–14442, https://doi.org/10.1021/jacs.9b07695.

[22] S. Wu, M. Li, H. Phan, D. Wang, T.S. Herng, J. Ding, Z. Lu, J. Wu, Toward two-dimensional π-conjugated covalent organic radical frameworks, Angew. Chem., Int. Ed. 57 (2015) 8007–8011, https://doi.org/10.1002/anie.201801998.

[23] Z. Mi, T. Zhou, W. Weng, J. Unruangsri, K. Hu, W. Yang, C. Wang, K.A.I. Zhang, J. Guo, Covalent organic frameworks enabling site isolation of viologen-derived electron-transfer mediators for stable photocatalytic hydrogen evolution, Angew. Chem. Int. Ed. 60 (2021) 9642–9649, https://doi.org/10.1002/anie.202016618.

[24] Y. Mu, Y. Liu, H. Tian, D. Ou, L. Gong, J. Zhao, Y. Zhang, Y. Huo, Z. Yang, Z. Chi, Sensitive and repeatable photoinduced luminescent radicals from a simple organic crystal, Angew. Chem. Int. Ed. 60 (2021) 6367–6371, https://doi.org/10.1002/anie.202014720.

[25] C.J. Zeman IV, S. Kim, F. Zhang, K.S. Schanze, Direct observation of the reduction of aryl halides by a photoexcited perylene diimide radical anion, J. Am. Chem. Soc. 142 (2020) 2204–2207, https://doi.org/10.1021/jacs.9b13027.

[26] F. Zhang, S. Wei, W. Wei, J. Zou, G. Gu, D. Wu, S. Bi, F. Zhang, Trimethyltriazine-derived olefin-linked covalent organic framework with ultralong nanofibers, Sci. Bull. 65 (2020) 1659–1666, https://doi.org/10.1016/j.scib.2020.05.033.

[27] L. Zhai, S. Yang, X. Yang, W. Ye, J. Wang, W. Chen, Y. Guo, L. Mi, Z. Wu, C. Soutis, Q. Xu, Z. Jiang, Conjugated covalent organic frameworks as platinum nanoparticle supports for catalyzing the oxygen reduction reaction, Chem. Mater. 32 (2020) 9747–9752, https://doi.org/10.1021/acs.chemmater.0c03614.

[28] M. Thommes, K. Kaneko, A.V. Neimark, J.P. Olivier, F. Rodriguez-Reinoso, J. Rouquerol, K.S.W. Sing, Physisorption of gases, with special reference to the evaluation of surface area and pore size distribution (IUPAC technical report), Pure Appl. Chem. 87 (2015) 1051–1069, https://doi.org/10.1515/pac-2014-1117.

[29] J.M. Rotter, R. Guntermann, M. Auth, A. Mahringer, A. Sperlich, V. Dyakonov, D. D. Medina, T. Bein, Highly conducting wurster-type twisted covalent organic frameworks, Chem. Sci. 11 (2020) 12843–12853, https://doi.org/10.1039/D0SC03909H.

[30] A.J. Sindt, B.A. DeHaven, D.F. McEachern, D.M.M. Dissanayake, M.D. Smith, A. K. Vannucci, L.S. Shimizu, UV-irradiation of self-assembled triphenylamines affords persistent and regenerable radicals, Chem. Sci. 10 (2019) 2670–2677, https://doi.org/10.1039/c8sc04607g.

[31] V. Lakshmi, C.-H. Liu, M.R. Rao, Y. Chen, Y. Fang, A. Dadvand, E. Hamzehpoor, Y. Sakai-Otsuka, R.S. Stein, D.F. Perepichka, A two-dimensional poly (azatriangulene) covalent organic framework with semiconducting and paramagnetic states, J. Am. Chem. Soc. 142 (2020) 2155–2160, https://doi.org/10.1021/jacs.9b11528.

[32] Y. Dai, W. Li, Z. Chen, X. Zhu, J. Liu, R. Zhao, D.S. Wright, A. Noori, M.F. Mousavi, C. Zhang, An air-stable electrochromic conjugated microporous polymer as an emerging electrode material for hybrid energy storage systems, J. Mater. Chem. A 7 (2019) 16397–16405, https://doi.org/10.1039/c9ta03001h.

[33] M. Lu, J. Liu, Q. Li, M. Zhang, M. Liu, J.-L. Wang, D.-Q. Yuan, Y.-Q. Lan, Rational crystalline covalent organic frameworks design for efficient CO_2 photoreduction with H_2O, Angew. Chem. Int. Ed. 58 (2019) 12392–12397, https://doi.org/10.1002/anie.201906890.

[34] K.-K. Chen, S. Guo, H. Liu, X. Li, Z.-M. Zhang, T.-B. Lu, Strong Visible-light-absorbing cuprous sensitizers for dramatically boosting photocatalysis, Angew. Chem. Int. Ed. 59 (2020) 12951–12957, https://doi.org/10.1002/anie.202003251.

[35] S. Li, L. Li, Y. Li, L. Dai, L.C. Liu, Y. Liu, J. Li, J. Lv, P. Li, B. Wang, Fully conjugated donor–acceptor covalent organic frameworks for photocatalytic oxidative amine

coupling and thioamide cyclization, ACS Catal. 10 (2020) 8717–8726, https://doi.org/10.1021/acscatal.0c01242.
[36] L.A. Mackenzie, L. Wang, N.P.R. Onuska, O.F. Williams, K. Begam, A.M. Moran, B. D. Dunietz, D.A. Nicewicz, Discovery and characterization of an acridine radical photoreductant, Nature 580 (2020) 76–80, https://doi.org/10.1038/s41586-020-2131-1.
[37] Y. Yang, H. Niu, L. Xu, H. Zhang, Y. Cai, Triazine functionalized fully conjugated covalent organic framework for efficient photocatalysis, Appl. Catal. B Environ. 269 (2020), 118799, https://doi.org/10.1016/j.apcatb.2020.118799.
[38] M. Ma, Z. Huang, D.E. Doronkin, W. Fa, Z. Rao, Y. Zou, R. Wang, Y. Zhong, Y. Cao, R. Zhang, Y. Zhou, Ultrahigh surface density of Co-N_2C single-atom-sites for boosting photocatalytic CO_2 reduction to methanol, Appl. Catal. B Environ. 300 (2022), 120695, https://doi.org/10.1016/j.apcatb.2021.120695.
[39] S. Yang, W. Hu, X. Zhang, P. He, B. Pattengale, C. Liu, M. Cendejas, I. Hermans, X. Zhang, J. Zhang, J. Huang, 2D Covalent organic frameworks as intrinsic photocatalysts for visible light-driven CO_2 reduction, J. Am. Chem. Soc. 140 (2018) 14614–14618, https://doi.org/10.1021/jacs.8b09705.
[40] D. Koyama, H.J.A. Dale, A.J. Orr-Ewing, Ultrafast observation of a photoredox reaction mechanism: photoinitiation in organocatalyzed atom-transfer radical polymerization, J. Am. Chem. Soc. 140 (2018) 1285–1293, https://doi.org/10.1021/jacs.7b07829.
[41] Z. Fu, X. Wang, A. Gardner, X. Wang, S.Y. Chong, G. Neri, A.J. Cowan, L. Liu, X. Li, A. Vogel, R. Clowes, M. Bilton, L. Chen, R.S. Sprick, A. Cooper, A stable covalent organic framework for photocatalytic carbon dioxide reduction, Chem. Sci. 11 (2020) 543–550, https://doi.org/10.1039/C9SC03800K.
[42] L. Tang, C. Fang, Nitration of tyrosine channels photoenergy through a conical intersection in water, J. Phys. Chem. B 123 (2019) 4915–4928, https://doi.org/10.1021/acs.jpcb.9b03464.
[43] C. Song, J. Nie, C. Ma, C. Lu, F. Wang, G. Yang, 1,2,3-Triazole-based conjugated porous polymers for visible light induced oxidative organic transformations, Appl. Catal. B Environ. 287 (2020), 119984, https://doi.org/10.1016/j.apcatb.2021.119984.
[44] X. Yu, S.M. Cohen, Photocatalytic metal–organic frameworks for the aerobic oxidation of arylboronic acids, Chem. Commun. 51 (2015) 9880–9883, https://doi.org/10.1039/C5CC01697E.
[45] Y.-T. Xu, C.-Y. Li, X.B. Huang, W.-X. Gao, Y.-B. Zhou, M.-C. Liu, H.-Y. Wu, Photoinduced hydroxylation of arylboronic acids with molecular oxygen under photocatalyst-free conditions, Green Chem. 21 (2019) 4971–4975, https://doi.org/10.1039/C9GC02229E.
[46] Y. Chen, J. Hu, A. Ding, Aerobic photooxidative hydroxylation of boronic acids catalyzed by anthraquinone-containing polymeric photosensitizer, RSC Adv. 10 (2020) 7927–7932, https://doi.org/10.1039/D0RA00176G.
[47] H. Hao, F. Zhang, X. Dong, X. Lang, 2D sp2carbon-conjugated triazine covalent organic framework photocatalysis for blue light-induced selective oxidation of sulfides with O_2, Appl. Catal. B Environ. 299 (2021), 120691, https://doi.org/10.1016/j.apcatb.2021.120691.
[48] K. Hosoi, Y. Kuriyama, S. Inagi, T. Fuchigami, Electrochemical hydroxylation of organoboron compounds, Chem. Commun. 46 (2010) 1284–1286, https://doi.org/10.1039/b914093j.
[49] Y.-X. Tan, S.-X. Lin, C. Liu, Y. Huang, M. Zhou, Q. Kang, D. Yuan, M. Hong, Boosting photocatalytic cross-dehydrogenative coupling reaction by incorporating $[Ru^{II}(bpy)_3]$ into a radical metal-organic framework, Appl. Catal. B Environ. 227 (2018) 425–432, https://doi.org/10.1016/j.apcatb.2018.01.048.
[50] W. Zhang, J. Tang, W. Yu, Q. Huang, Y. Fu, G. Kuang, C. Pan, G. Yu, Visible light-driven C-3 functionalization of indoles over conjugated microporous polymers, ACS Catal. 8 (2018) 8084–8091, https://doi.org/10.1021/acscatal.8b01478.